Journal of Nuclear Medicine, published on February 17, 2022 as doi:10.2967/jnumed.121.263310

Radium 223 induces transient functional bone marrow toxicity

Maria Parlani[1,*], Francesco Boccalatte[2,*], Anna Yeaton[2], Feng Wang[3], Jianhua Zhang[3], Iannis Aifantis[2], Eleonora Dondossola[1]

[1] David H. Koch Center for Applied Research of Genitourinary Cancers and Genitourinary Medical Oncology Department, The University of Texas (UT) MD Anderson Cancer Center, Houston, TX, 77030, USA;

[2] Department of Pathology and Laura and Isaac Perlmutter Cancer Center, New York University School of Medicine, New York, NY, 10016, USA;

[3] Department of Genomic Medicine, UT MD Anderson Cancer Center, Houston, TX, 77030, USA

* M.P. and F.B. contributed equally to this study

Corresponding authors:

Eleonora Dondossola, UT MD Anderson Cancer Center, Houston, 1515 Holcombe Blvd, TX 77030, USA; phone number, +1 7137459200; email: EDondossola@mdanderson.org

Francesco Boccalatte, New York University School of Medicine, 550 First Avenue, New York, NY 10016, USA; phone number, +1 2122639262; email: francesco.boccalatte@nyulangone.org;

First author:

Maria Parlani, UT MD Anderson Cancer Center, Houston, 1515 Holcombe Blvd, TX 77030, USA; phone number, +1 7137459200; present email: Maria.Parlani@radboudumc.nl

Keywords: Radium 223, myelotoxicity, bone marrow

Running title: ^{223}Ra-induced transient myelotoxicity

ABSTRACT

Radium 223 (^{223}Ra) is a bone-seeking, α–particle-emitting radionuclide approved for the treatment of patients with metastatic prostate cancer and is currently being tested in a variety of clinical trials for primary and metastatic cancers to bone.

Clinical evaluation of ^{223}Ra hematologic safety showed a significantly increased rate of neutropenia and thrombocytopenia in patients, hinting at myelosuppression as a side effect. In this study we investigate the consequences of ^{223}Ra treatment on bone marrow biology.

^{223}Ra accumulated in bones and induced zonal radiation damage confined at the bone interface, followed by replacement of the impaired areas with adipocyte infiltration, as monitored by three-dimensional multiphoton microscopy, ex vivo. Flow cytometry and single cell transcriptomic analyses on bone marrow hematopoietic populations revealed transient, non-specific ^{223}Ra-mediated cytotoxicity on resident populations, including stem, progenitor and mature leukocytes. This was paralleled by a significant decrease of white blood cells and platelets in peripheral blood, which was overcome within 40 days post-treatment. ^{223}Ra exposure did not impair full hematopoietic reconstitution, suggesting that the bone marrow function is not permanently hampered.

Our results provide a comprehensive explanation of ^{223}Ra reversible effects on bone marrow cells and exclude long-term myelotoxicity, supporting its safety for patients.

GRAPHICAL ABSTRACT

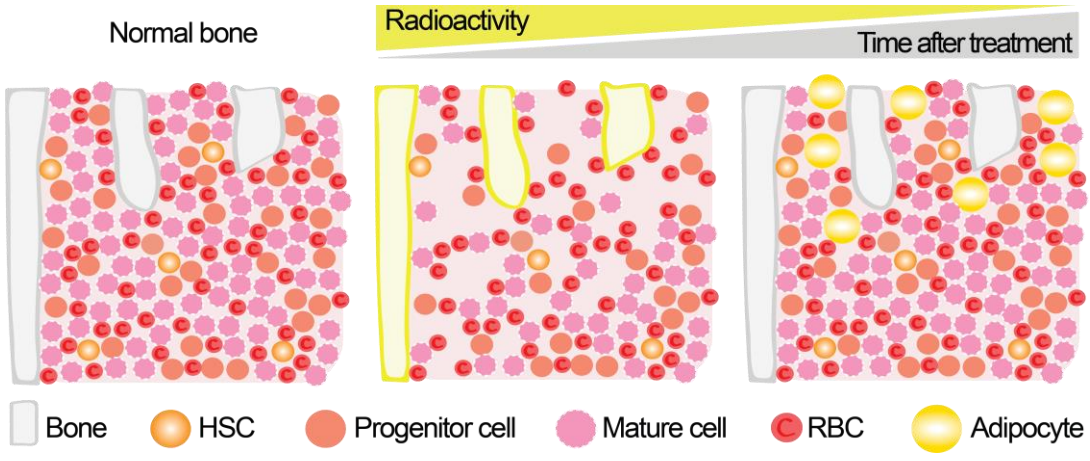

INTRODUCTION

Radium 223 (^{223}Ra) is an α–particle emitter that accumulates in bone after *in vivo* administration (*1,2*). This radioisotope has been originally tested as targeted radiotherapy for prostate cancer (PCa) metastasis in bone (*1*), which represents a major site for distant colonization (*3*). The high energetic radiation of ^{223}Ra coupled to limited penetrance in tissues (<100 μm) mediates zonal toxicity at the bone interface towards osteoblasts, osteoclasts and tumor cells *(4-7)*. ^{223}Ra prolonged the median overall survival (3.6 months) and delayed the time to first symptomatic skeletal event (5.8 months) in men afflicted with metastatic PCa to bone (*8,9*). These results led to the approval of ^{223}Ra for the treatment of metastatic PCa patients with symptomatic bone lesions and no visceral involvement (*8,9*). Based on this positive outcome, the use of ^{223}Ra is now being clinically investigated for other tumor types that colonize the bone, including multiple myeloma, hormone-positive breast cancer, renal cell carcinoma, non-small cell lung cancer and differentiated thyroid cancer (*10-12*).

Follow up studies conducted in patients excluded long-term emergence of secondary malignancies associated to ^{223}Ra treatment (such as other primary bone cancers or acute myelogenous leukemia) for up to 3-years (*13,14*). Hematologic safety analyses, instead, showed an impact by ^{223}Ra on bone marrow function (*15*). Accordingly, median absolute neutrophil counts and platelet number, which remained constant for placebo-treated patients, significantly decreased in ^{223}Ra-treated men, with a rebound after the end of the treatment. Hemoglobin levels, instead, were not significantly affected over the treatment period in both ^{223}Ra and placebo groups. In comparison, antitumor radiation levels of β-emitting agents such as Strontium 89 or Samarium 153 ethylenediamine-tetra-methylene-phosphonic acid, which displays abundant γ-emission, are associated with more severe bone marrow toxicity, which limits their usefulness for treating patients (*1*).

Neutropenia and thrombocytopenia currently represent the most common adverse reactions and hint at significant levels of bone marrow toxicity (*15*). Therefore, understanding the biological determinants of ^{223}Ra-mediated myelosuppression and the medium/long-term consequences on bone marrow function is critical to support a more meaningful and rational application of this agent in current

and future patients. Furthermore, ruling out major toxic effects could further prompt ^{223}Ra use in early stage patients.

In this study we investigated the effects of ^{223}Ra on bone marrow biology, including topology and function. We applied preclinical murine models combined with three-dimensional (3D) multiphoton microscopy, flow cytometry analysis, bone marrow transplantation experiments and single cell RNA-sequencing to elucidate ^{223}Ra-mediated myelotoxicity over time.

MATERIALS AND METHODS

Animal Studies. Animal studies were approved by the Institutional Animal Care and Use Committee of UT MD Anderson Cancer Center and performed according to the institutional guidelines for animal care and handling. Details on in vivo studies are provided in Supplemental Information.

Statistical Analysis. Statistical analysis was performed using GraphPad Prism 8 by unpaired two-tailed Student's t test or one-way analysis of variance (ANOVA) followed by Tukey's post hoc test. Data are means ± SD. For scRNA-seq, differential expression analysis was determined by using the Wilcoxon rank sum test.

Further experimental methods are detailed in the Supplementary Methods.

RESULTS

^{223}Ra Accumulates in Bones and Affects the Bone Marrow Compartment

In order to study the effects of ^{223}Ra on bone marrow biology, C57BL/6 mice were administered with a single dose of 7.5 KBq, according to the therapeutic dosage used in other preclinical analyses in mice (*2,4,6*). Radiation emission was monitored up to 40 days in femur, tibia, humerus, skull and spine. ^{223}Ra accumulated in different bones and significantly decayed over time at a similar extent, with limited radiation emission ($\leq$15% of the initial amount) detectable by day 40 post-injection, in line with its half-life of 11.4 days (*1*) (Fig. 1A). Bone matrix showed localized radioactivity, whereas no signal was detected within bone marrow cells (Fig. 1A). These results confirm that ^{223}Ra accumulates in calcified bone tissues but not in the bone marrow cavity, as previously reported (*2*). Interestingly, ^{223}Ra

induced a significant decrease of white blood cells in bone, while levels of red blood cells and platelets did not significantly change (Fig. 1B). These results suggest that ^{223}Ra incorporates in the calcified component of bone and induces cellular changes in bone marrow cells.

^{223}Ra Induces Topological Changes within the Bone Marrow Cavity

Next, we investigated the topologic effects that ^{223}Ra exerts over time on bone marrow cells by applying infrared-excited nonlinear microscopy. We focused on tibia that recapitulates the complexity of bone architecture, including areas of cancellous bone at the distal epiphysis/metaphysis (where ^{223}Ra effects should be maximized (*2*)), and a trabecular-free cavity at the diaphysis (where the impact of ^{223}Ra should be minimal (*2*)). Tibiae were processed, cut at the vibratome to generate 3D slices, stained and analyzed by multiphoton microscopy. We acquired 3D stacks (up to 4.5 mm x 1.2 mm x 200 µm) at different time points and monitored bone marrow cells (CD45, a marker expressed by all nucleated hematopoietic cells (*16*), and DAPI), together with second and third harmonic generation (SHG, THG), two label-free nonlinear imaging techniques. SHG is elicited by non-centrosymmetric structure, such as collagen deposited in the bone matrix (*4*), while THG is engendered at different interfaces, such water-lipid interface in adipocytes (*17*). Bone marrow at the baseline showed a homogenous distribution of CD45^{+} cells, intercalated within bone trabeculae at the epiphysis and metaphysis, with no evidence of adipocytes, as expected for healthy adult mice younger than 2 years (*18*) (Fig. 2A; Supplemental Fig. 1A). By day 4 post-^{223}Ra injection, bone marrow at the epiphysis and metaphysis showed major damage, with CD45^{+} cells alternated to strongly fluorescent circular structures, negative for THG (Fig. 2A; Supplemental Fig. 1B). These events preferentially localized at 36.6$\pm$36 µm of distance from bone, either trabecular or cortical and distributed mostly at the epiphysis or metaphysis, within 1.39 mm (Fig. 2B) of distance from the growth plate. By day 11, active damage persisted in proximity to cancellous and cortical bone, with preferential distribution at 2247$\pm$700 µm distance from the growth plate, paralleled by the emergence of THG-positive adipocytes at the epiphysis and metaphysis (Fig. 2; Supplemental Fig. 1C). This trend increased up to day 40 (Fig. 2A; Supplemental Fig. 1D), with a significantly higher number of THG-positive adipocytes at the epiphysis and metaphysis and some

damage still persisting at the metaphysis (Fig. 2B). By day 60, less than 5 areas of damage per slice were still visible, with a significant infiltration of adipocytes at the epiphysis and metaphysis (Fig. 2B; Supplemental Fig. 1E). The bone marrow at the diaphysis, instead, did not show any sign of perturbation, even at day 4 post-treatment, when the damage was more evident in other areas (Fig. 2; Supplemental Fig. 1A-E). Progressive adipocyte increase at the epiphysis and metaphysis, with no involvement of the diaphysis, was further confirmed by histology (Supplemental Fig. 2).

These results suggest that ^{223}Ra induces extensive bone marrow remodeling at the epiphysis and metaphysis, which are more exposed to its radiation, possibly due to the presence of cancellous bone, but leave the diaphysis morphologically unperturbed.

^{223}Ra Induces Transient, Non-specific Myelotoxicity in Bone Marrow-derived Cells

To evaluate the effects of ^{223}Ra on specific bone marrow populations, mice were treated with ^{223}Ra and their bone marrow collected either before (d0) or after 4, 11 and 40 days post-treatment. Then, the impact of ^{223}Ra on stem, progenitor, mature leukocyte and erythroid cells was evaluated by flow cytometry (Supplemental Fig. 3; Supplemental Table 1). ^{223}Ra treatment significantly depleted total $CD45^+$ bone marrow leukocytes at 4 and 11 days post-treatment, while their number returned to baseline after 40 days, indicating a transient effect (Fig. 3A; Supplemental Fig. 4A). To further evaluate the long-term toxicity, we monitored hematopoietic stem and progenitor cells at various stages of differentiation and found that the early myeloid and lymphoid lineages were affected at a similar extent (Fig. 3A; Supplemental Fig. 4B, C). Notably, also the long-term hematopoietic stem cell (HSC) population ($Lin^-Kit^+Sca^+CD135^-CD150^+CD40^-$) was significantly reduced by ^{223}Ra, but fully recovered 40 days after treatment, suggesting restoration of the hematopoiesis and reversible myelotoxicity. This was further confirmed by the evaluation of mature myeloid and lymphoid cells, that reached normal levels 40 days after treatment (Fig. 3A; Supplemental Fig. 4D). The only cell type not significantly affected by ^{223}Ra treatment was represented by mature erythrocytes. To better understand the nature of this phenomenon, we further dissected this population according to the maturation stages and identified depletion of the more immature precursors and erythroblasts (Ery A) by early ^{223}Ra treatment,

while the mature, non-nucleated erythrocytes (EryC, which are the most abundant population) were unaffected by ^{223}Ra (Fig. 3A; Supplemental Fig. 4E). The absence of splenomegaly up to day 40 post-treatment suggests that no extramedullary hematopoiesis emerged to compensate the bone marrow functional damage (Fig. 3B). Analysis of peripheral blood at different time points post-^{223}Ra treatment showed a significant decrease of white blood cells up to day 28 and of platelets up to day 16 post-treatment, and no significant reduction of red blood cells, hemoglobin or hematocrit (Fig. 3C), in agreement with the outcome observed in patients (*15*).

These results indicate that treatment with ^{223}Ra has a widespread toxicity on multiple bone marrow populations, which resolves over time. In order to evaluate the global effects of ^{223}Ra on bone marrow early hematopoietic populations, we conducted single-cell RNA sequencing (scRNA-seq) on Kit^{+} hematopoietic stem and progenitor cells (HSPCs) from the bone marrow of C57BL/6 mice over time (day 0, 4, 11 and 40 post-treatment with ^{223}Ra; n=3 mice/time-point). We obtained high quality transcriptomic data from a total of 10501 single cells followed by analysis by using Seurat, an R package designed for scRNA-seq data (*19*). The distribution of all the transcriptomes over time was visualized using the Uniform Manifold Approximation and Projection (UMAP) method (Fig. 4A). To define similarity clusters, we applied unsupervised clustering based on the differential expression analysis for specific genes with a resolution of 0.8 and resolved 26 separate clusters (Supplemental Fig. 5 and 6). Based on previous studies on single-cell gene expression *(20)*, we manually curated population-specific genes in each cluster and defined 16 distinct populations, comprising all major stem, progenitor and mature bone marrow cell types (Fig. 4A). In particular, to guide a reliable cell type assignment, we examined the expression of specific genes correlating with a more primitive (CD34, Flt3) or more lineage-primed (Dntt, Elane, Ly6g) phenotype (Fig. 4B and Supplemental Fig. 7). By comparing the bone marrow composition at baseline and after ^{223}Ra treatment over time, we observed that the most primitive cluster of HSPC (made of 796 single cells and quite homogenous in terms of differential gene expression) underwent a limited proportional skewing, while lineage-primed precursors showed either a contraction (e.g., granulocytic and neutrophil precursors) or an expansion (e.g. CMP, B cell precursors and progenitors). These adaptations were prevalently limited to the initial timepoints

after ^{223}Ra treatment, while the reciprocal proportions were re-established within 40 days from treatment (Figure 4C), in line with flow cytometry data. To leverage the power of single-cell transcriptome data, we then examined differentially expressed genes (DEGs) from the clusters representing stem and early progenitors by comparing each post-treatment timepoint (d4, d11, d40) to the baseline (d0). Gene ontology and pathway search via Gene Set Enrichment Analysis (*21-23)* at day 4 post-treatment showed upregulation of genes related to apoptosis, radiation response and double-strand break repair, reflecting an ionizing insult and need to react, which in HSPC was overcome by day 40. An enrichment for terms related to metabolism, DNA replication, cell cycle and hematopoietic stem/progenitor cell differentiation was also evident in most populations at early time points (Fig. 4D), indicating that the acute irradiation insult prompted progenitor cells to activate a mitogenic program to restore all hematopoietic types to their baseline levels. Interestingly, very few differences were identifiable at baseline and 40 days after treatment (Fig. 4D, Supplemental Fig. 8) in more immature populations, indicating that most perturbations at the transcriptomic level are fully resolved.

Overall, the data obtained at the single-cell level indicate an acute toxicity of ^{223}Ra on all bone marrow populations, which is overcome by 40 days after treatment. This supports the notion that ^{223}Ra administration, although acutely toxic, does not cause permanent damage to the hematopoietic system.

^{223}Ra Exposure Does Not Impair Full Hematopoietic Reconstitution

Given the transient myelotoxicity that affects all the hematopoietic compartments, we further investigated whether HSCs were able to fully reconstitute a functional steady-state hematopoiesis after acute exposure to ^{223}Ra. To this purpose, we performed bone marrow transplantation experiments using bone marrow from donors which were exposed to ^{223}Ra treatment. C57BL/6 GFP mice were treated with saline (as control) or ^{223}Ra; after 30 days their bone marrow was recovered and implanted in lethally irradiated wild type C57BL/6 mice. 3D reconstruction of femurs at the multiphoton microscope one month after treatment showed repopulation of the bone marrow cavity by GFP cells in both control and ^{223}Ra-exposed mice, while wild type C57BL/6 mice did not show any specific fluorescence (Fig. 5A). Hematological parameters (white blood cells, red blood cells, hemoglobin, platelets) were

monitored as an index of functional bone marrow reconstitution 1 month-post transplantation, showing no differences between mice that were previously exposed to ^{223}Ra or control treatment (Fig. 5B). Finally, both control or ^{223}Ra-exposed mice survived 40 weeks post-transplantation (Fig. 5C).

These results show that the acute ^{223}Ra insult to HSCs does not impair a full hematopoietic reconstitution, thus indicating that the treatment is not subverting bone marrow function in the long-term.

DISCUSSION

Among the limited treatments currently available for patients affected by metastatic castration resistant PCa to bone, ^{223}Ra is a viable option that improves overall survival coupled to good therapeutic index and relatively low toxicity (*8*). Such results prompted further clinical testing of ^{223}Ra for the treatment of other primary and metastatic cancers to bone, with an increasing number of patients that could benefit from this drug (*10-12*).

^{223}Ra exerts zonal cancer cell killing and efficiently reduce tumor mass *in vivo*, especially in the case of small lesions (*4,7*) and its preventive application decreases tumor burden in preclinical models of disseminated breast cancer (*10*). In addition, retrospective clinical analyses showed that overall survival is improved in men with metastatic bone disease and a low bone scan index (*24*), while recent preliminary clinical observations suggest that ^{223}Ra has higher efficiency in individuals with fewer circulating tumor cells (CTCs; <5 CTCs/7.5 ml of blood) (*25*). Altogether, this evidence supports ^{223}Ra application for secondary prevention of bone metastasis and treatment of oligometastatic bone disease to achieve maximal efficacy, extending the benefits of this treatment to patients at early stages.

Recent clinical observations showed that ^{223}Ra does not induce the emergence of secondary malignancies (*13,14*), while neutropenia and thrombocytopenia are among the most common side effects (*15*). To exclude long-term myelotoxicity, which is particularly relevant when considering a larger cohort of patients with longer survival expectancy, we tested the global effects of ^{223}Ra exposure on hematopoiesis in preclinical models. We confirmed that ^{223}Ra incorporation within bone calcified matrix induces cellular changes in the bone marrow. Topological alterations were induced in the bone marrow

cavity, where zonal radio-damage emerged 4 days post-treatment and decreased over time up to day 40 post-treatment, paralleled by an increment of adipocytes. Cytotoxicity, which extended among all hematopoietic cell lineages, was overcome by 6 weeks from ^{223}Ra administration and paralleled by a significant, transient decrease of circulating white blood cells, with a 50% reduction 28 days post-treatment compared to control-treated mice. In patients, 4 weeks after the first dose of ^{223}Ra, the levels of circulating neutrophils significantly decrease of ~25% (*15*). The higher cytotoxic impact in mouse models might be explained by the smaller scale of bones compared to human ones, which in proportion are exposed to higher levels of α-radiation (that travels for <100 µm of distance (*8*)).

Blood cell formation occurs in a complex microenvironment where a number of different stromal cell types (such as endothelial, osteoblastic and adipogenic progenitors) foster hematopoiesis through mutual interactions. This delicate balance is compromised by external insults, such as chemotherapy or radiation (*18*), which impact the hematopoietic compartment both directly (by arresting its proliferation) and indirectly (by compromising its niche (*26-28*)). ^{223}Rad induces zonal bone marrow injury at the tibia epiphysis and metaphysis, paralleled by the transient change in the number of peripheral blood cells. This early damage is followed by a marked increase of adipocytes, which usually accompanies the restoration of normal hematopoiesis. This is in line with recent studies showing that irradiation or fluorouracil treatment causes the differentiation of stromal cells into adipocytes, which in turn produce cytokines that stimulate HSCs to regenerate hematopoiesis (*20*). Bone marrow alterations were evident at the epiphysis or metaphysis, where dense trabecular areas are present and more prominent bone remodeling of cancellous bone (*29*) could further increase ^{223}Ra incorporation, enhancing zonal toxicity. On the contrary, the diaphysis was relatively unaltered. Consistently, high resolution analysis of bone by α–camera autoradiography showed a predominant ^{223}Ra localization at the growth plate, with little activity at the diaphysis and no signal from the bone marrow (*2*). Interestingly, the majority of quiescent long term-HSCs preferentially reside in the diaphysis, and in particular within perivascular rather than osteoblastic niches (*30*), suggesting a potential role for the regional-specific distribution of ^{223}Ra in sparing some niches which host HSCs.

Importantly, our results show no major differences in lineage commitment at baseline and 40 days post-^{223}Ra treatment, neither in the transcriptional programs of the HSPCs nor in their mature progeny. The bone marrow of mice exposed to ^{223}Ra efficiently restores full hematopoiesis in irradiated hosts, with no significant differences compared to control-treated mice. This suggests that, despite a transient bone marrow damage, HSC functionality and normal hematopoietic reconstitution processes are not permanently impaired by ^{223}Ra. Our study addressed these effects after exposure to one therapeutic dose of ^{223}Ra and follow up work can be further performed to exclude a potential increased cytotoxicity by repeated cycles of treatment or to exposure to higher doses.

CONCLUSIONS

In conclusion, our results provide a comprehensive explanation to the effects of ^{223}Ra on bone marrow cells and suggests their reversibility, excluding long-term myelotoxicity.

ACKNOWLEDGMENTS

We wish to thank Drs. Maria Guillamot-Ruano and Lara Brambilla (NYU Langone Health) for critical reading of the manuscript and the Leukemia Sample Bank at UT MD Anderson Cancer Center for sharing the ABX Micros 60 instrument.

Funding: UT MD Anderson Cancer Center Prostate Cancer SPORE (P50 CA140388–09) and Moonshots Initiative; Bayer HealthCare Pharmaceuticals (57440); US National Institutes of Health (R01CA202025, R01CA202027, R01CA216421, R01CA228135; P01CA229086 and P30 CA016672), Leukemia & Lymphoma Society (TRP#6580); Alex's Lemonade Stand Foundation for Childhood Cancer; St. Baldrick's Cancer Research Foundation. ^{223}Ra is from Bayer. The funders did not have any influence on any aspects of the study, including design, data collection, analyses, interpretation, or writing the manuscript. No potential conflicts of interest relevant to this article exist.

KEY POINTS

QUESTION: Is ^{223}Ra inducing permanent bone marrow damage?

PERTINENT FINDINGS: ^{223}Ra prolongs survival in bone metastatic patients but induces significant levels of neutropenia**.** 3D multiphoton microscopy, FACS analysis, single cell RNA sequencing, and bone marrow transplant reveal reversible ^{223}Ra-mediated functional myelotoxicity.

IMPICATIONS FOR PATIENT CARE: Our results provide a comprehensive explanation of ^{223}Ra reversible effects on bone marrow cells and exclude long-term myelotoxicity, supporting its safety for patients.

REFERENCES

1. Bruland OS, Nilsson S, Fisher DR, Larsen RH. High-linear energy transfer irradiation targeted to skeletal metastases by the alpha-emitter 223ra: Adjuvant or alternative to conventional modalities? *Clin Cancer Res*. 2006;12:6250s-6257s.

2. Abou DS, Ulmert D, Doucet M, Hobbs RF, Riddle RC, Thorek DL. Whole-body and microenvironmental localization of radium-223 in naive and mouse models of prostate cancer metastasis. *J Natl Cancer Inst*. 2015; 108:djv380.

3. Gandaglia G, Abdollah F, Schiffmann J, et al. Distribution of metastatic sites in patients with prostate cancer: A population-based analysis. *Prostate*. 2014;74:210-6.

4. Dondossola E, Casarin S, Paindelli C, et al. Radium 223-mediated zonal cytotoxicity of prostate cancer in bone. *J Natl Cancer Inst*. 2019; 111:1042-1050.

5. Paindelli C, Navone N, Logothetis CJ, Friedl P, Dondossola E. Engineered bone for probing organotypic growth and therapy response of prostate cancer tumoroids in vitro. *Biomaterials*. 2019;197:296-304.

6. Suominen MI, Fagerlund KM, Rissanen JP, et al. Radium-223 inhibits osseous prostate cancer growth by dual targeting of cancer cells and bone microenvironment in mouse models. *Clin Cancer Res*. 2017;23:4335-4346.

7. Paindelli C, Casarin S, Wang F, et al. Enhancing radium 223 treatment efficacy by anti-beta 1 integrin targeting. *J Nucl Med*. 2021;jnumed.121.262743.

8. Parker C, Nilsson S, Heinrich D, et al. Alpha emitter radium-223 and survival in metastatic prostate cancer. *N Engl J Med*. 2013;369:213-23.

9. Sartor O, Coleman R, Nilsson S, et al. Effect of radium-223 dichloride on symptomatic skeletal events in patients with castration-resistant prostate cancer and bone metastases: Results from a phase 3, double-blind, randomised trial. *Lancet Oncol*. 2014;15:738-46.

10. Suominen MI, Rissanen JP, Kakonen R, et al. Survival benefit with radium-223 dichloride in a mouse model of breast cancer bone metastasis. *J Natl Cancer Inst*. 2013;105:908-16.

11. Ueno NT, Tahara RK, Fujii T, et al. Phase ii study of radium-223 dichloride combined with hormonal therapy for hormone receptor-positive, bone-dominant metastatic breast cancer. *Cancer Med*. 2020;9:1025-1032.

12. Morris MJ, Corey E, Guise TA, et al. Radium-223 mechanism of action: Implications for use in treatment combinations. *Nat Rev Urol*. 2019;16:745-756.

13. Parker CC, Coleman RE, Sartor O, et al. Three-year safety of radium-223 dichloride in patients with castration-resistant prostate cancer and symptomatic bone metastases from phase 3 randomized alpharadin in symptomatic prostate cancer trial. *Eur Urol*. 2018;73:427-435.

14. Dizdarevic S, Petersen PM, Essler M, et al. Interim analysis of the reassure (radium-223 alpha emitter agent in non-intervention safety study in mcrpc population for long-term evaluation) study: Patient characteristics and safety according to prior use of chemotherapy in routine clinical practice. *Eur J Nucl Med Mol Imaging*. 2019;46:1102-1110.

15. Vogelzang NJ, Coleman RE, Michalski JM, et al. Hematologic safety of radium-223 dichloride: Baseline prognostic factors associated with myelosuppression in the alsympca trial. *Clin Genitourin Cancer*. 2017;15:42-52.e8.

16. Hermiston ML, Zikherman J, Zhu JW. Cd45, cd148, and lyp/pep: Critical phosphatases regulating src family kinase signaling networks in immune cells. *Immunol Rev*. 2009;228:288-311.

17. Tsai C-K, Wang T-D, Lin J-W, et al. Virtual optical biopsy of human adipocytes with third harmonic generation microscopy. *Biomed Opt Express*. 2013;4:178-186.

18. Naveiras O, Nardi V, Wenzel PL, Hauschka PV, Fahey F, Daley GQ. Bone-marrow adipocytes as negative regulators of the haematopoietic microenvironment. *Nature*. 2009;460:259-63.

19. Butler A, Hoffman P, Smibert P, Papalexi E, Satija R. Integrating single-cell transcriptomic data across different conditions, technologies, and species. *Nat Biotech*. 2018;36:411-420.

20. Giladi A, Paul F, Herzog Y, et al. Single-cell characterization of haematopoietic progenitors and their trajectories in homeostasis and perturbed haematopoiesis. *Nat Cell Biol*. 2018;20:836-846.

21. Hänzelmann S, Castelo R, Guinney J. Gsva: Gene set variation analysis for microarray and rna-seq data. *BMC Bioinformatics*. 2013;14:7.

22. Liberzon A, Birger C, Thorvaldsdóttir H, Ghandi M, Mesirov JP, Tamayo P. The molecular signatures database (msigdb) hallmark gene set collection. *Cell Syst*. 2015;1:417-425.

23. Barbie DA, Tamayo P, Boehm JS, et al. Systematic rna interference reveals that oncogenic kras-driven cancers require tbk1. *Nature*. 2009;462:108-12.

24. Alva A, Nordquist L, Daignault S, et al. Clinical correlates of benefit from radium-223 therapy in metastatic castration resistant prostate cancer. *Prostate*. 2017;77:479-488.

25. Carles J, Castellano D, Méndez-Vidal MJ, et al. Circulating tumor cells as a biomarker of survival and response to radium-223 therapy: Experience in a cohort of patients with metastatic castration-resistant prostate cancer. *Clin Genitourin Cancer*. 2018;16:e1133-e1139.

26. McCulloch EA, Till JE. The radiation sensitivity of normal mouse bone marrow cells, determined by quantitative marrow transplantation into irradiated mice. *Rad Res*. 1960;13:115-125.

27. Xie Y, Yin T, Wiegraebe W, et al. Detection of functional haematopoietic stem cell niche using real-time imaging. *Nature*. 2009;457:97-101.

28. Otsuka K, Hirabayashi Y, Tsuboi I, Inoue T. Regeneration capability of lin-/c-kit+/sca-1+ cells with or without radiation exposure for repopulation of peripheral blood in lethally irradiated mice monitored using ly5.1 isotype on days 35, 90, and 270 after transplantation. *Exp Hematol*. 2010;38:417-25.

29. Langdahl B, Ferrari S, Dempster DW. Bone modeling and remodeling: Potential as therapeutic targets for the treatment of osteoporosis. *Ther Adv Musculoskelet Dis*. 2016;8:225-235.

30. Acar M, Kocherlakota KS, Murphy MM, et al. Deep imaging of bone marrow shows non-dividing stem cells are mainly perisinusoidal. *Nature*. 2015;526:126-30.

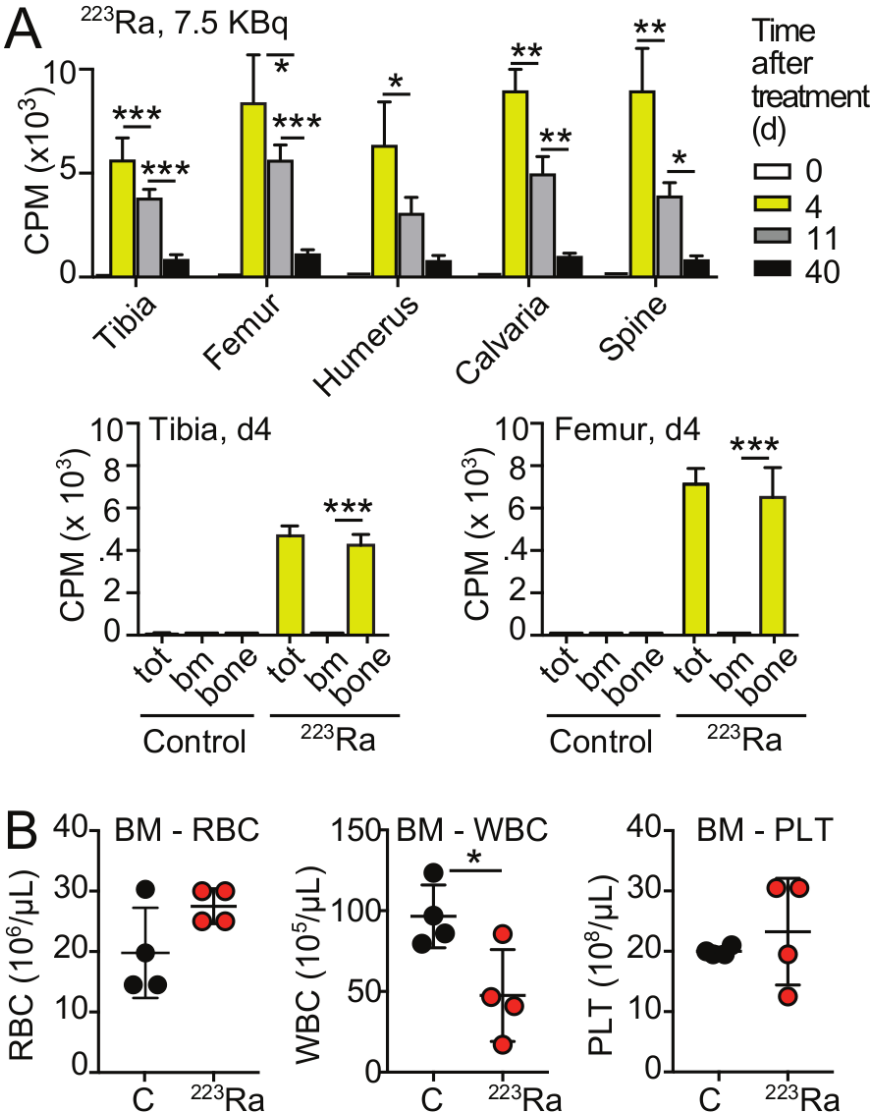

Fig. 1. ^{223}Ra accumulates in bones and affects the bone marrow compartment. (A) Measurement of radiation emission by ^{223}Ra-treated bones over time. Tibia, femur, humerus, calvaria and spine were removed at 0, 4, 11 or 40 days-post ^{223}Ra treatment and counts per minute (CPM) measured. Mean ± SD is shown, n=3-6 bones/group. *p<0.05, **p<0.01, ***p<0.001, one-way ANOVA followed by Tukey's HSD post-hoc test. Tibia and femur from control mice or 4 days post-^{223}Ra treatment were removed and CPM measured for total bone or mineralized bone and bone marrow separately, after bone marrow flushing. Mean ± SD is shown, n=4 bones/group. ***p<0.001 by unpaired two-tailed Student's t test. (B) Bone marrow hematological analysis of control and ^{223}Ra (d4) treated mice by ABX Micros 60 hematology analyzer. BM, bone marrow; WBC, white blood cells; RBC, red blood cells; PLT, platelets. Mean ± SD is shown, n=4 mice/group. *p<0.05 by unpaired two-tailed Student's t test.

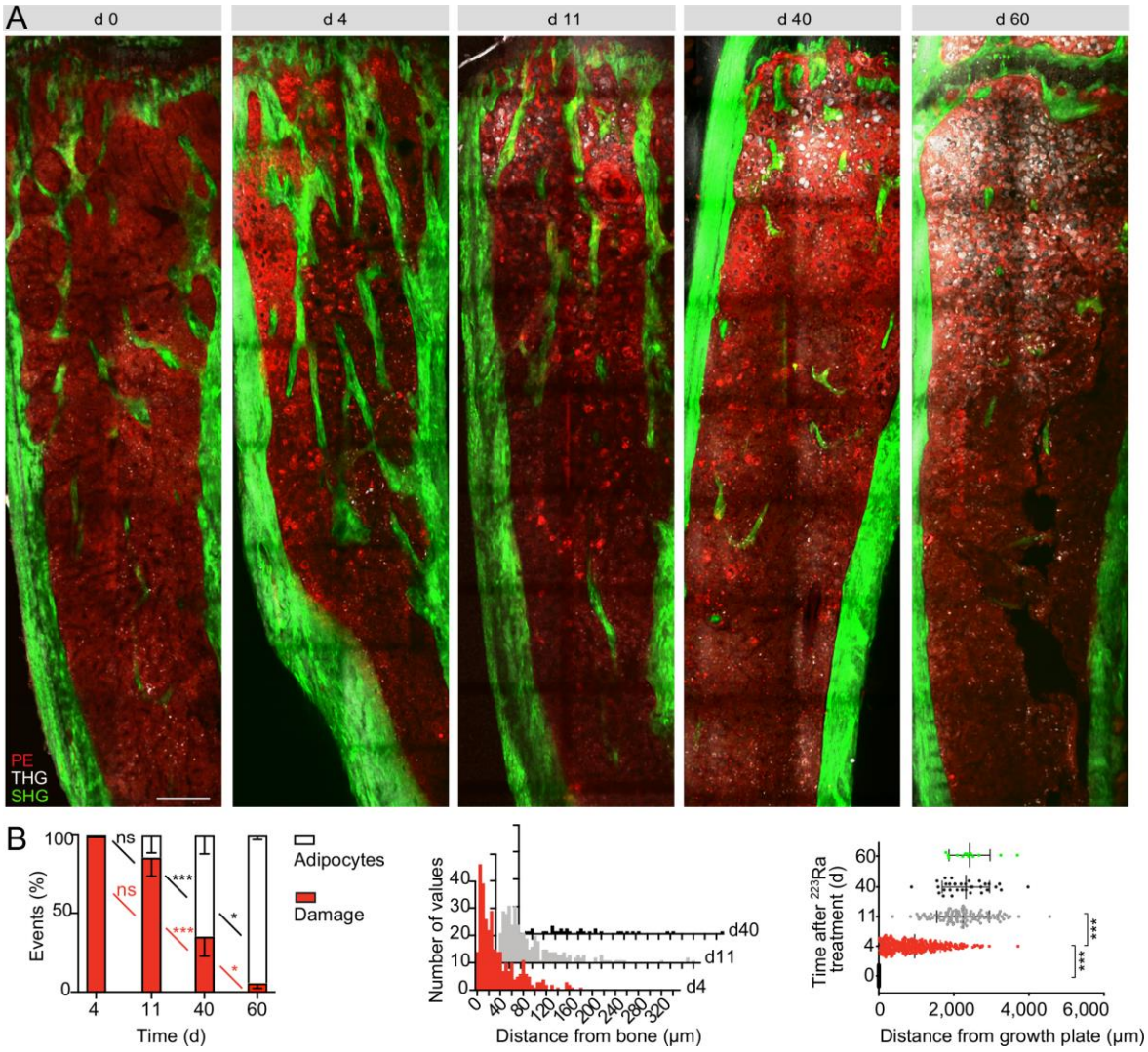

Fig. 2. ^{223}Ra induces topological changes within the bone marrow cavity. (A) Immunofluorescence analysis of 4.5 mm x 1.2 mm x 200 µm tibia slices retrieved from mice before and 4, 11, 40 and 60 days post-^{223}Ra treatment. CD45^{+} cells, PE, red; adipocytes, third harmonic generation (THG), grey; bone, second harmonic generation (SHG), green. Scale bar, 300 µm. (B) Percentage of radiation damage events and adipocytes in the tibia slices at day 0-60 post-^{223}Ra treatment. Mean ± SD is shown, the total number of events is reported for n=1 slices/tibia, 1 tibia/mouse, 3 mice/group. (C) Frequency distribution of radiation damage event distance from bone at day 4, 11 and 40. n=1 slices/tibia, 1 tibia/mouse, 3 mice/group. (D) Distance of radiation damage events from the growth plate at day 0-60 post-^{223}Ra treatment. Mean ± SD is shown, the total number of events is reported for n=1 slices/tibia, 1 tibia/mouse, 3 mice/group. *p<0.05, ***p<0.001, one-way ANOVA followed by Tukey's HSD post-hoc test.

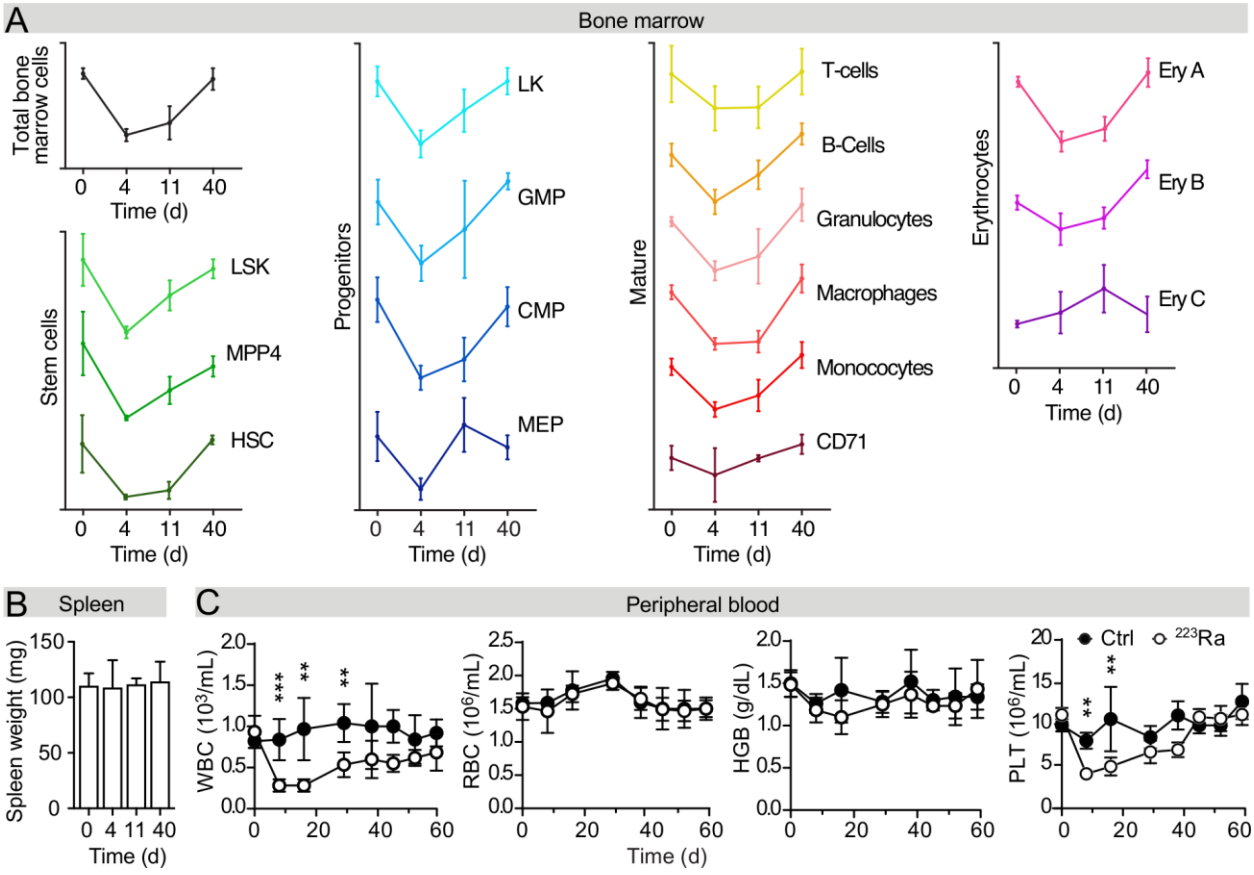

Fig. 3. ^{223}Ra causes a significant but transient myelotoxicity. (A) Effects of ^{223}Ra treatment at baseline and after 4, 11 and 40 days on total bone marrow leukocytes; HSPCs (based on LSK, MPP4 or HSC markers); early progenitor cells (based on LK, GMP, CMP, MEP markers); B, T, myeloid and erythroid markers and erythroid cells at different stages of maturation; n=3-4 mice/group; one representative experiment is shown; the experiment was repeated twice. Absolute numbers for each graph and statistical analysis are reported in Supplemental Fig. 4. (B) Spleen weight, n=4 spleens/group. (C) Hematological analysis of control and ^{223}Ra-treated mice at day 0-60 post-treatment. WBC, white blood cells; RBC, red blood cells; HGB, hemoglobin; HCT, hematocrit; PLT, platelets; n=5-6 mice/group; one representative experiment is shown, the experiment was repeated twice. **p<0.01, ***p<0.001 by unpaired two-tailed Student's t test.

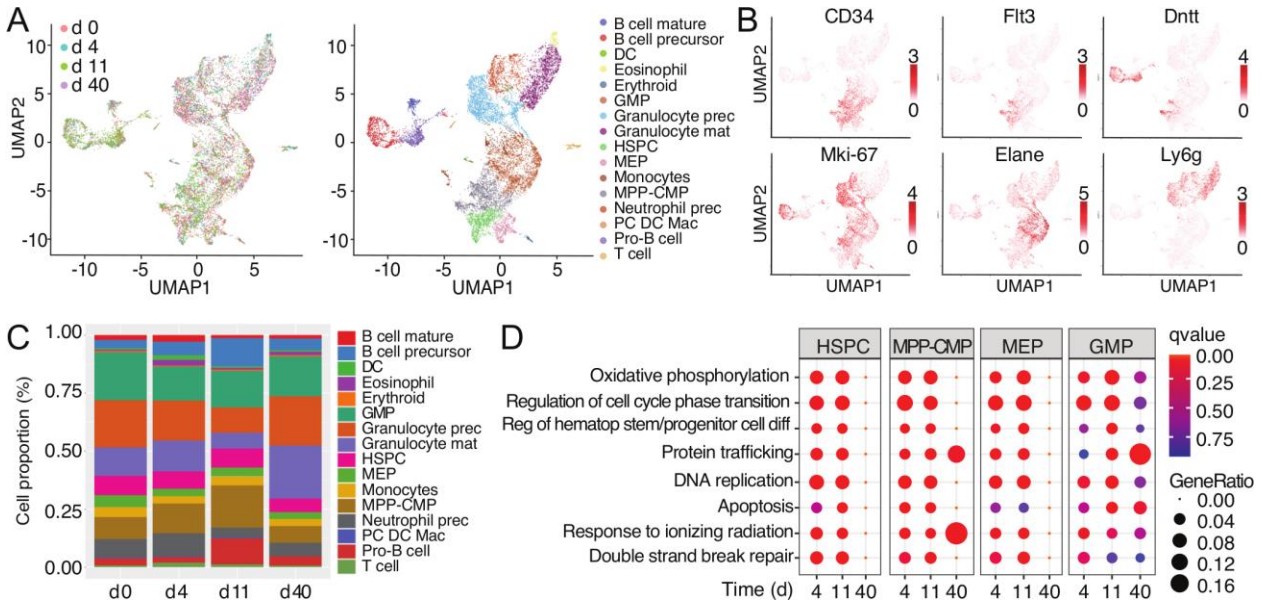

Fig. 4. ^{223}Ra treatment induces temporary changes on bone marrow cells transcriptome. (A) UMAP plot of scR NA-seq data collected from Kit+ bone marrow cells of C57/BL6 mice before treatment (d0) and after 4, 11, 40 days (d4, d11, d40) of treatment with ^{223}Ra (n=3 mice per group). (B) UMAP plot of color-coded hematopoietic populations, based on single cell transcriptomic profiles. (C) Expression pattern of selected key marker genes. The color scale indicates the log normalized expression levels of the indicated genes. (D) Relative proportion of 16 individual cell populations overtime after treatment with ^{223}Ra for 0 (untreated), 4, 11 and 40 days. (E) Dot plots showing the most representative gene-sets from the top differentially expressed genes in mice treated with ^{223}Ra for 4, 11 and 40 days versus untreated (d0). The size of the dots represents the proportion of differential expressed genes in each term, while the color indicates the significance of the enrichment.

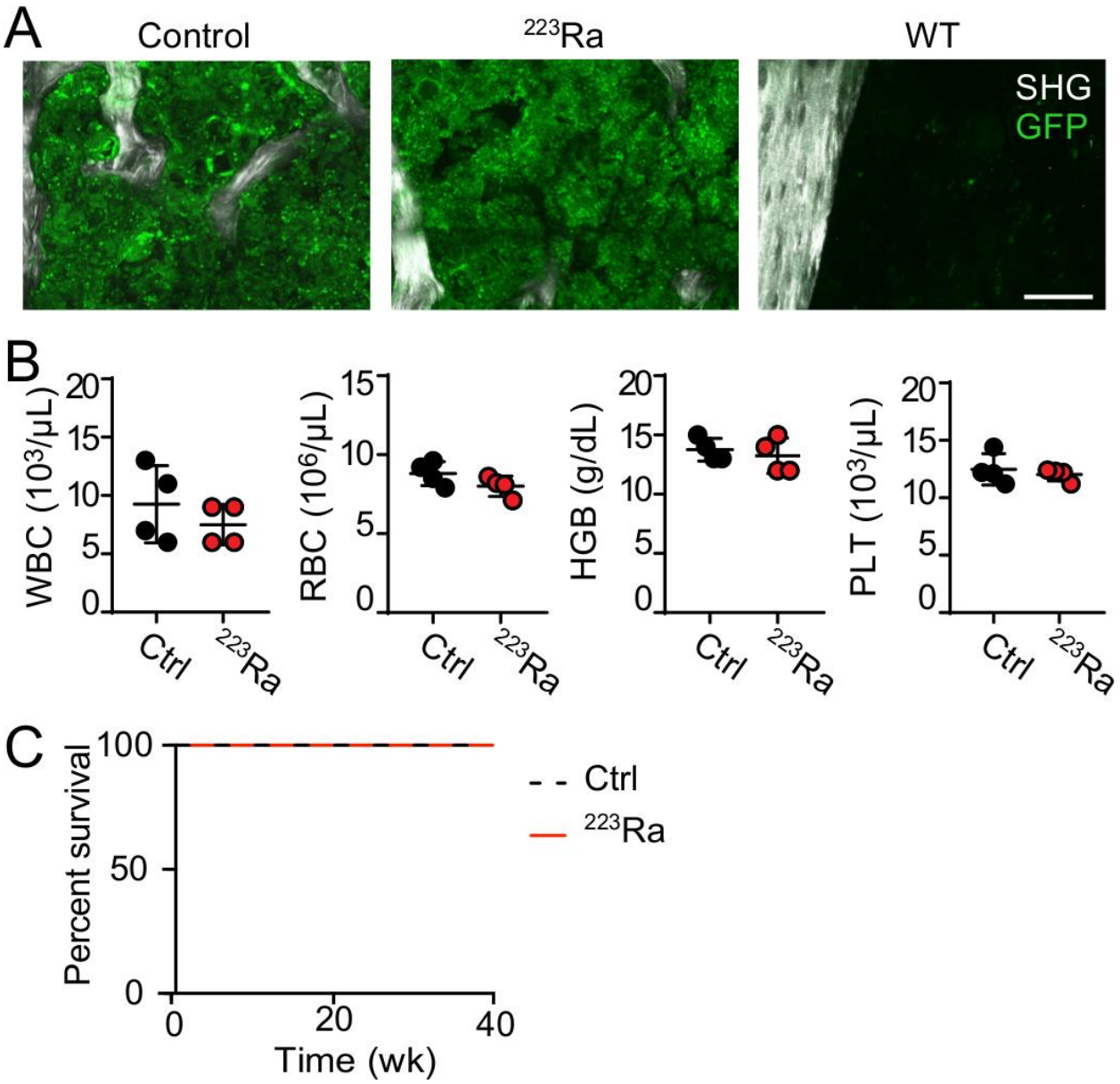

Fig. 5. ^{223}Ra does not affect long term functionality of hematopoietic stem cells. (A) Bone marrow reconstitution in mice administered with control or ^{223}Ra exposed bone marrow cells monitored by immunofluorescence analysis 1 month post-transplantation. A wild type (WT)-GFP mouse tibia is shown as negative control. Scale bar, 100 μm. (B) Hematological analysis of transplanted mice. WBC, white blood cells; RBC, red blood cells; HGB, hemoglobin; PLT, platelets. Mean ± SD is shown, n=4 mice/group. (C) Survival of control or ^{223}Ra-exposed transplanted mice, n=4.

Supplemental Materials and methods

Animal studies. Animal studies were approved by the Institutional Animal Care and Use Committee of The University of Texas, MD Anderson Cancer Center, which is accredited by the Association for Assessment and Accreditation of Laboratory Animal Care. >12-weeks old C57BL/6 male mice were purchased from the Department of Experimental Radiation Oncology, M.D. Anderson Cancer Center; C57BL/6-Tg (UBC-GFP) 30Scha/J were from Jackson Lab. Mice were housed with a maximum of 5 animals per cage in a state-of-the-art, air-conditioned, specific-pathogen–free animal facility and all procedures were performed in accordance with the NIH Policy on Humane Care and Use of Laboratory Animals. Treatments and retro-orbital bleeds were performed on mice under general anesthesia (isoflurane). Animals were observed daily and examined by a veterinarian 5 days/week for signs of morbidity (e.g. matted fur, weight loss, limited ambulation, and respiratory difficulty). In case of discomfort, the animals were euthanized by asphyxiation with carbon dioxide gas followed by cervical dislocation, consistent with the recommendations of the Panel on Euthanasia of the American Veterinary Medical Association.

Single-cell library preparation and sequencing. Bone marrow was collected at d0, d4, d11, d40 from ^{223}Ra treatment. After sorting for CD117^{+} cells from 3 mice/timepoint, each timepoint was tagged with oligo-tagged antibodies to uniquely label cells from distinct samples (https://cite-seq.com/cell-hashing/). Samples were pooled and single-cell RNA-seq libraries were prepared using Single Cell 3′ Reagent Kits v.2: Chromium Single Cell 3′ Library & Gel Bead Kit v.2, PN-120237; Single Cell 3′ Chip Kit v.2 PN-120236; and i7 Multiplex Kit PN-120262 (10x Genomics) following the Single Cell 3′ Reagent Kits v.2 User Guide (Manual Part no. CG00052 Rev A). Libraries were run on an Illumina NovaSeq 6000 system as 150-bp paired-end reads, one full lane per sample.

Single-cell sequencing analysis. Sequencing results were demultiplexed and converted to FASTQ format using Illumina bcl2fastq software. The Cell Ranger Single-Cell Software Suite (https://support.10xgenomics.com/single-cell-gene-expression/ software/pipelines/latest/what-is-cell-ranger) was used to perform sample demultiplexing, barcode processing and single-cell 3′ gene counting.

We calculated the average expression levels of all genes across all cells of each cluster and used the gene set variation analysis package (XX) to determine cluster- level gene set enrichment scores of the relevant gene signatures. The scores were computed with the single-sample Gene Set Enrichment Analysis method (YY) The scores were normalized by the absolute difference between the minimum and the maximum, and plotted in a heatmap.

Bone harvesting and processing. Mice were euthanized and tibias removed at different time points: day 0 (before starting the treatment), 4, 11, 40, 60 post-treatment. Bones were cleaned from muscle tissue and fixed in 4% paraformaldehyde in a horizontal shaker with gentle agitation at 4 °C, overnight. Samples were then washed with Phosphate-buffered saline (PBS) three times and incubated for 4 days in 0.5 M ethylenediaminetetraacetic acid solution, pH 7.5, at 4 °C on a horizontal shaker with gentle agitation.

Vibratome sectioning and immunofluorescence staining. Tibiae were embedded in 4% UltraPure™ Agarose and sectioned in slices of 300 µm of thickness with a Leica VT1000S vibratome. Sections were incubated in staining solution (10% dimethyl sulfoxide, 0.5% IgePal630, 10% normal goat serum, in PBS) for 24 hours, followed by incubation with anti-mouse CD45 PE-conjugated antibody (1:50 in 200 µl of staining solution) and with 4′,6-diamidino-2-phenylindole (DAPI, 1:200 in 200 µl of staining solution) overnight. Sections were then washed in PBS for 24 hours (with several PBS changes) and analyzed at the multiphoton microscope. Stained sections

were fixed for 1h with 4% paraformaldehyde at room temperature and then stored in PBS in the dark at 4 °C.

3D image acquisition. Slices previously stained were acquired by non-linear multiphoton microscopy. A custom-made multiphoton microscope with three different titanium-sapphire lasers and two optical parametric oscillators (yielding a tunable range of excitation wavelengths between 800 and 1300 nm) was employed (LaVision BioTec) *(15)*. Multi-spectral detection of 3D stacks was performed using up to five photomultipliers and three excitation wavelengths in consecutive scans, to separate the following excitation and emission channels: third harmonic generation (THG, 1280 nm; 450/60 nm); phycoeritrin (PE, 1090 nm; 595/40 nm), second harmonic generation (SHG, 1090 nm; 525/50 nm), DAPI (1090 nm; 387/15 nm). A long-working distance ×16 numerical aperture 0.8 water objective (Olympus) was used. The three-dimensional (3D) stacks acquired were characterized by the same constant physical spatial resolutions of 625 x 625 µm (1064 x 1064 px) and penetration depth of 5 µm step-size, reaching up to maximum 200 µm. Images from individual 3D stacks were reconstructed and analyzed using NIH Image J. Adjacent 3D scan fields, each representing z-projections, were stitched to generate large-field overviews. Radiation damage-induced events and adipocytes were counted manually.

Flow Cytometry. Single-cell suspensions were generated by mechanical disruption of mouse bone marrow in PBS supplemented with 2% fetal bovine serum (FBS). For peripheral blood analysis, red blood cells were lysed as described above. Nonspecific antibody binding was blocked by incubation with 20 µg/ml rat IgG (Sigma) for 10 min. Cells were incubated with primary antibodies overnight, then washed in PBS and resuspended in PBS containing 2µg/ml DAPI to assess viability where indicated, otherwise PBS containing 2% FBS was used. The antibodies used in this study are listed in Supplemental Table 1. Lineage-negative cells were defined by lack of expression of Gr-1, TER-119, CD4, CD8, B220 and CD11b. Stained cells were quantified using

a BD Fortessa analyzer (Becton Dickinson). FlowJo software (Becton Dickinson) was used to generate flow cytometry plots and calculate percentages.

Retro-orbital bleeding and blood analysis. Prior to blood collection, mice were anesthetized using 3-4% isoflurane. When the mouse was fully asleep, a heparinized capillary tube was inserted into the medial canthus of the eye to puncture the tissue and enter in the sinus. Once the required volume of blood was collected (~100 µl in a tube with 10µl ethylenediaminetetraacetic acid solution) the capillary tube was removed, and the bleeding stopped by applying a gentle pressure with a gauze sponge. The blood collected was then diluted 1:10 in PBS and analyzed for leukocyte counts and blood parameters on an ABX Micros 60 hematology analyzer or by flow cytometry. For analysis of hematological parameters in bone marrow samples, bone marrow was collected by flushing it in 1 ml of PBS and analyzed on the ABX Micros 60 hematology analyzer.

Quantification of radio-emission in bone and bone marrow. Mice were euthanized and bones (tibia, femur, humerus, calvaria, vertebra) removed at day 0, 4, 11 or 40 post-treatment. The emission of radiation was measured with a Geiger counter in intact bones and, at day 4, in intact bones and calcified matrix or bone marrow after flushing. The bone marrow was flushed into 2 ml tubes by injection of 1.8 ml of PBS + 2% FBS (450 µl, 4 times, inverting the bone each time) using a syringe with a 27G needle. The whole bone marrow was flushed out from the bone cavity and no material was lost during the processing. The radioactivity of the calcified bone and the flushed bone marrow was measured with a Geiger counter.

Supplemental Table 1. List of antibodies used in flow cytometry

Antigen	Conjugate	Clone	Dilution	Manufacturer	Catalog #
CD4	APC-Cy7	RM4-5	1:500	Biolegend	100526
CD8a	APC-Cy7	53-6.7	1:500	Biolegend	100714
CD11b	APC-Cy7	M1/70	1:500	Biolegend	101226
Gr-1 (Ly-6C/6G)	APC-Cy7	RB6-8C5	1:500	Biolegend	108424
CD45R (B220)	APC-Cy7	RA3-6B2	1:500	Biolegend	103224
Ly-6C	APC-Cy7	HK1.4	1:300	Biolegend	128026
Ter-119	APC-Cy7	Ter-119	1:400	BD	560509
CD135	PE	A2F10.1	1:100	BD	553842
CD71	PE	RI7217	1:400	Biolegend	113808
CD11b	PE	M1/70	1:100	BD	553311
CD117	APC	2B8	1:400	Biolegend	105812
Sca1 (Ly-6A/E)	PE-Cy7	D7	1:400	Biolegend	108114
CD45	PE-Cy7	30-F11	1:400	Biolegend	103114
CD4	PE-Cy7	GK1.5	1:200	Biolegend	100422
CD8a	PE-Cy7	53-6.7	1:200	BD	552877
CD150	AlexaFluor488	TC15-12F12.2	1:200	Biolegend	115916
Cd34	FITC	RAM34	1:200	eBioscience	11-0341-82
Cd71	FITC	R17217	1:200	Biolegend	113806
CD48	Pac blue	HM48-1	1:200	Biolegend	103418
FcgR (Cd16/32)	eFluor450	93	1:200	eBioscience	48-0161-82
CD45R (B220)	Pac blue	RA3-6B2	1:200	BD	558108
Ly-6G	BV605	1A8	1:300	Biolegend	127639

Supplemental Figures

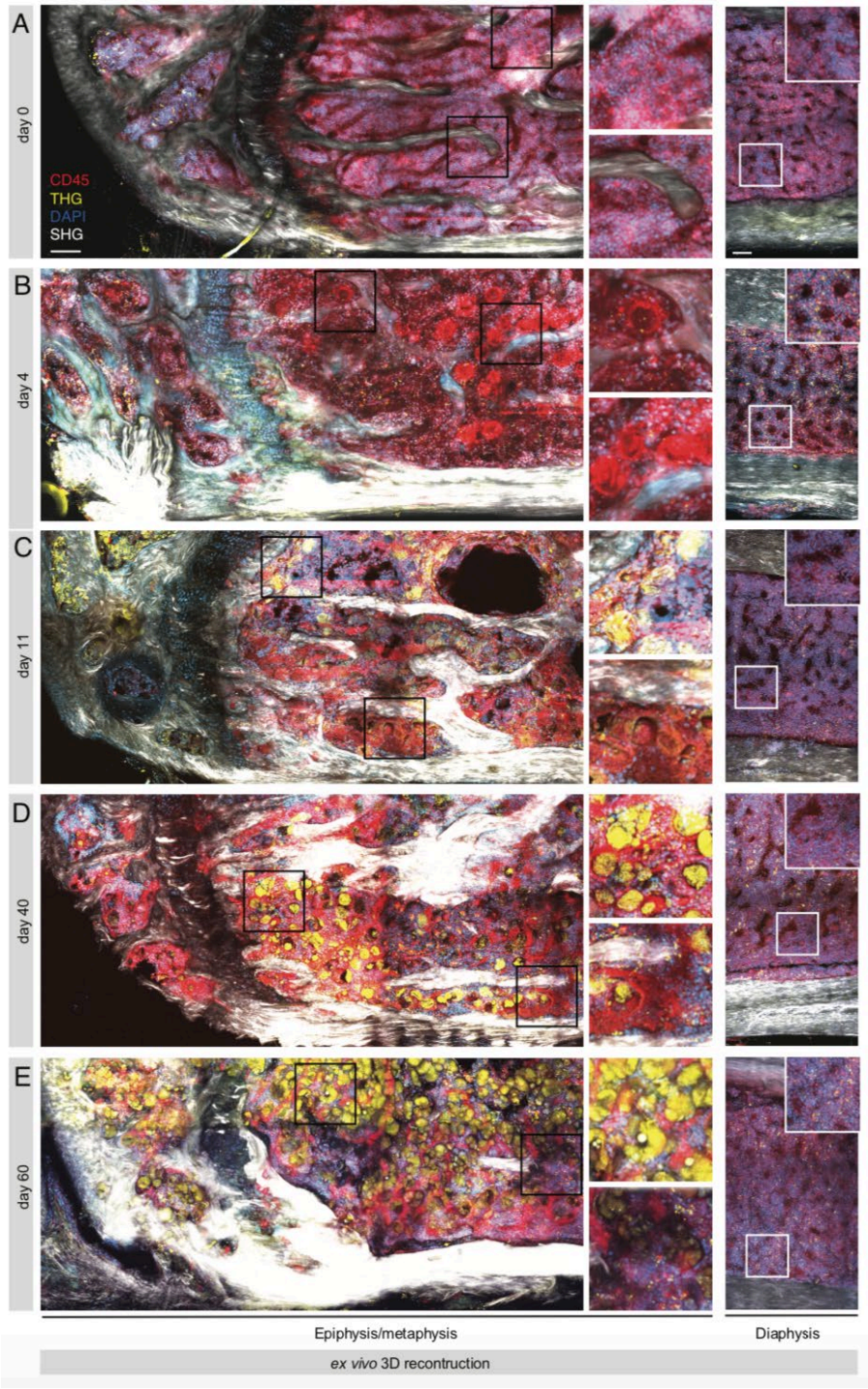

Supplemental Figure 1. Topological changes within the bone marrow cavity, details. (A-E) Immunofluorescence analysis of 300 µm-thick slices of tibiae retrieved from mice before (A) and 4 (B), 11 (C), 40 (D) and 60 (D) days post-^{223}Ra treatment. CD45^{+} cells, PE, red; adipocytes, third harmonic generation (THG), yellow; bone, second harmonic generation (SHG), gray; nuclei, DAPI, blue. Scale bar, 100 µm.

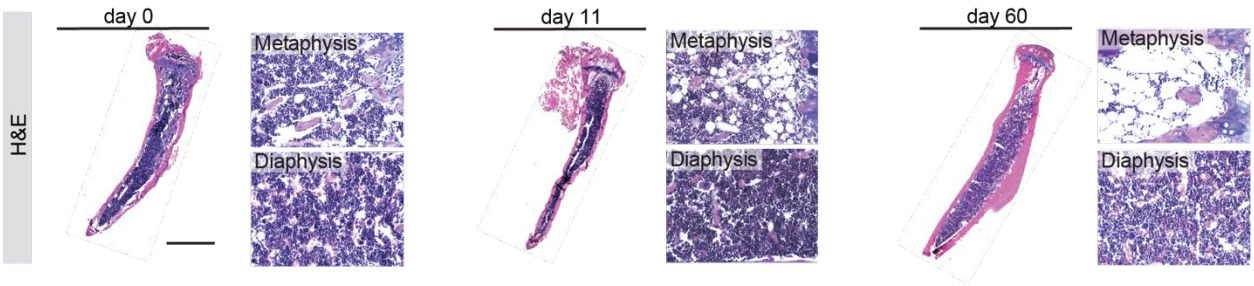

Supplemental Figure 2. ^{223}Ra induces topological changes within the bone marrow cavity, H&E staining of tibiae at day 0, 11 and 60 post-^{223}Ra treatment. Details of the epiphysis and diaphysis of each bone are shown. Scale bar, 500 µm.

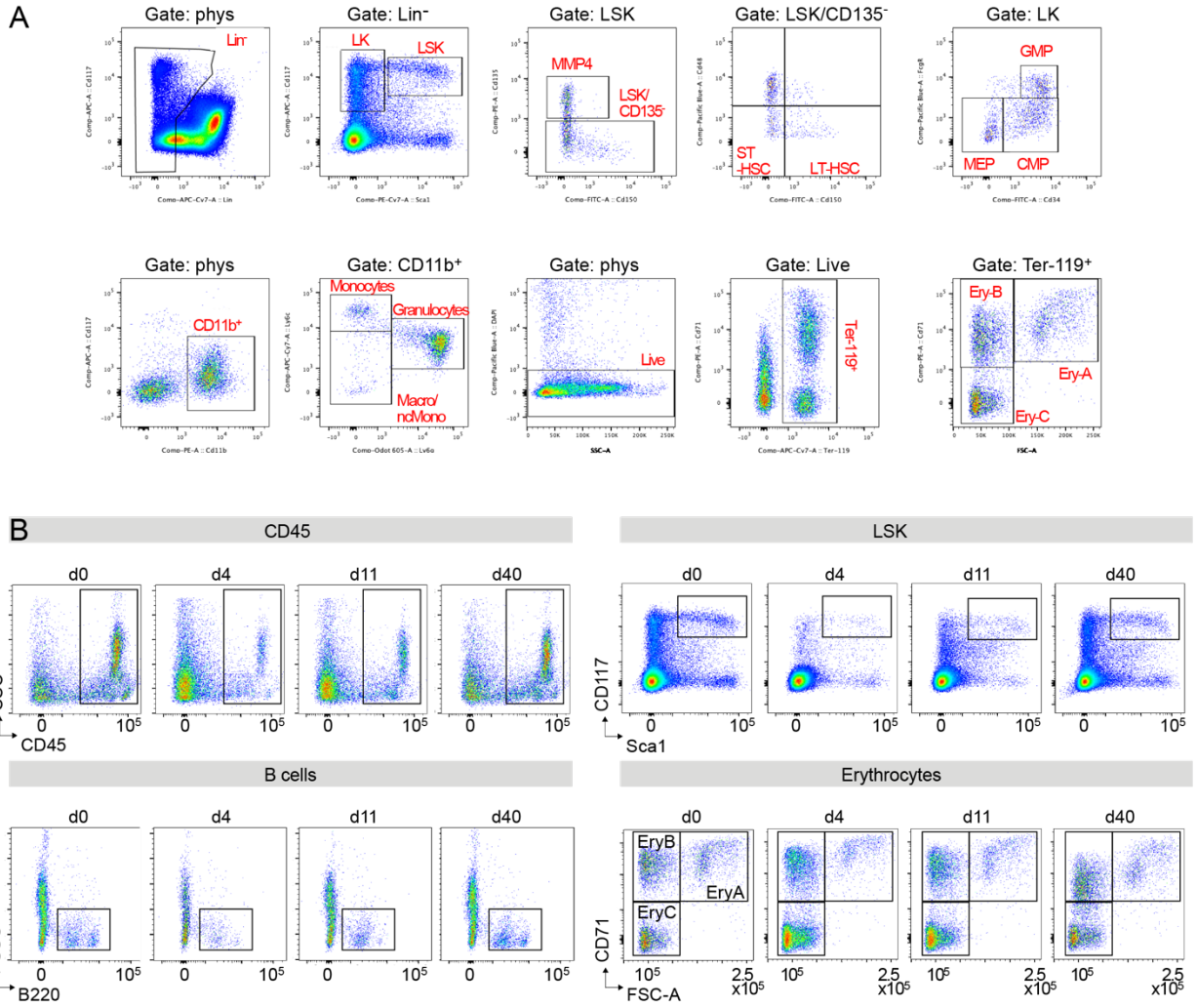

Supplemental Figure 3. Gating strategies for mouse BM. (A) Flow cytometry plots showing sequential gating for stem (A), progenitor (B), mature myeloid (C) and erythroid (D) cells. All panels were initially gated based on physical parameters (FSC/SSC), single cells (SSC-Area vs -Height) and live cells (DAPI-negative). (B) Representative flow cytometry plots illustrating the effects of ^{223}Ra administration on bone marrow leukocytes (by CD45 staining), stem/progenitor cells (by LSK staining), mature B cell (B220) and erythroid (Ter119/CD71) populations before or after 4, 11 and 40 days from treatment.

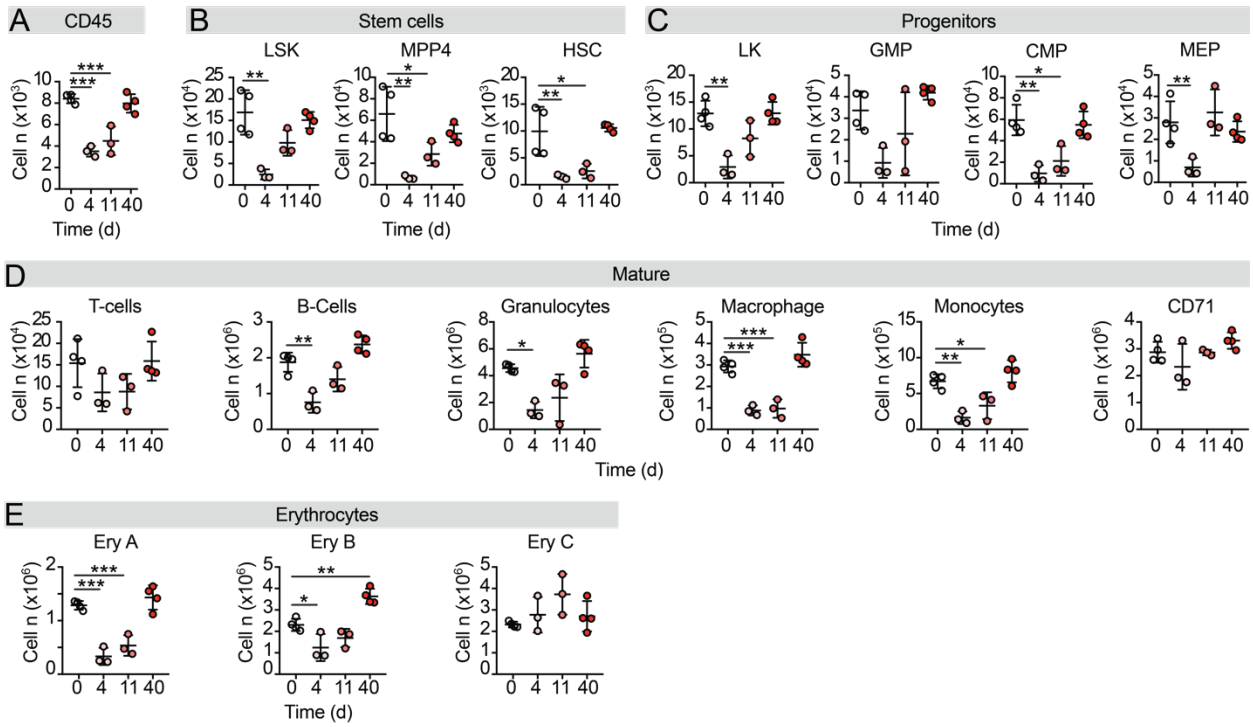

Supplemental Figure 4. ^{223}Ra causes a significant but transient myelotoxicity. (A) Absolute number of bone marrow leukocytes at baseline and after 4, 11 and 40 days from ^{223}Ra treatment. (B) Absolute number of bone marrow HSPCs (based on LSK, MPP4 or HSC markers). (C) Absolute number of bone marrow early progenitor cells (based on LK, GMP, CMP, MEP markers). (D) Absolute number of mature bone marrow cells, based on B, T, Myeloid and Erythroid markers. (E) Absolute number of bone marrow erythroid cells at different stages of maturation; n=3-4 mice/group; one representative experiment is shown; the experiment was repeated twice. *p<0.05, **p<0.01, ***p<0.001, one-way ANOVA followed by Tukey's HSD post-hoc test.

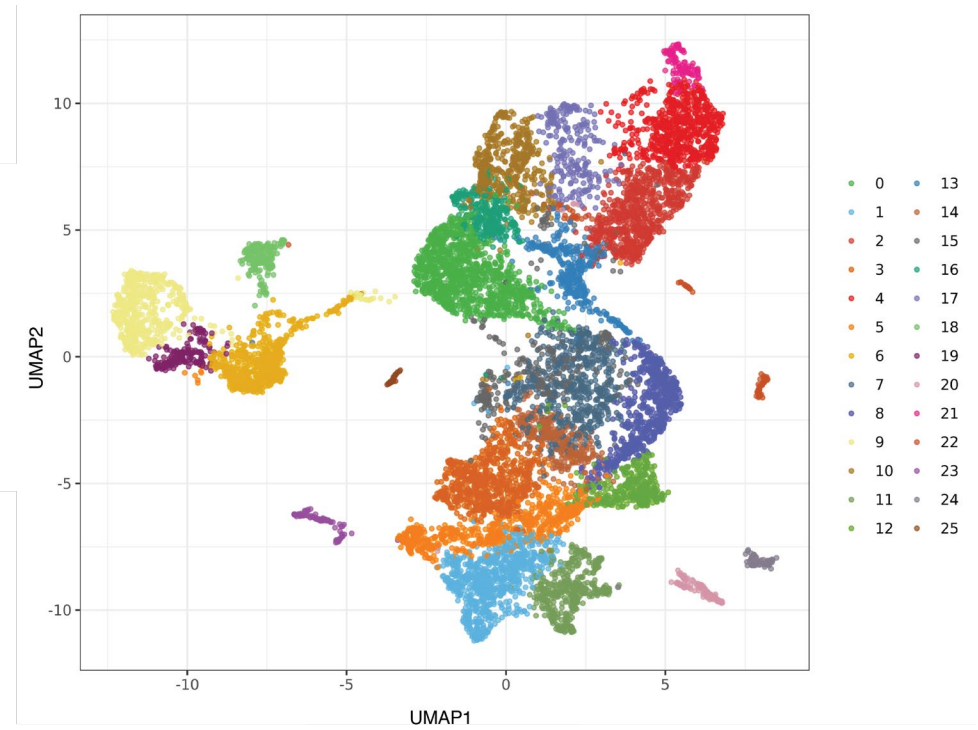

Supplemental Figure 5. scRNA-seq analysis of mouse bone marrow upon ^{223}Ra treatment. UMAP plot from the unsupervised clustering of differentially expressed genes in each cluster relative to other clusters with a resolution of 0.8, which resolved 26 individual clusters.

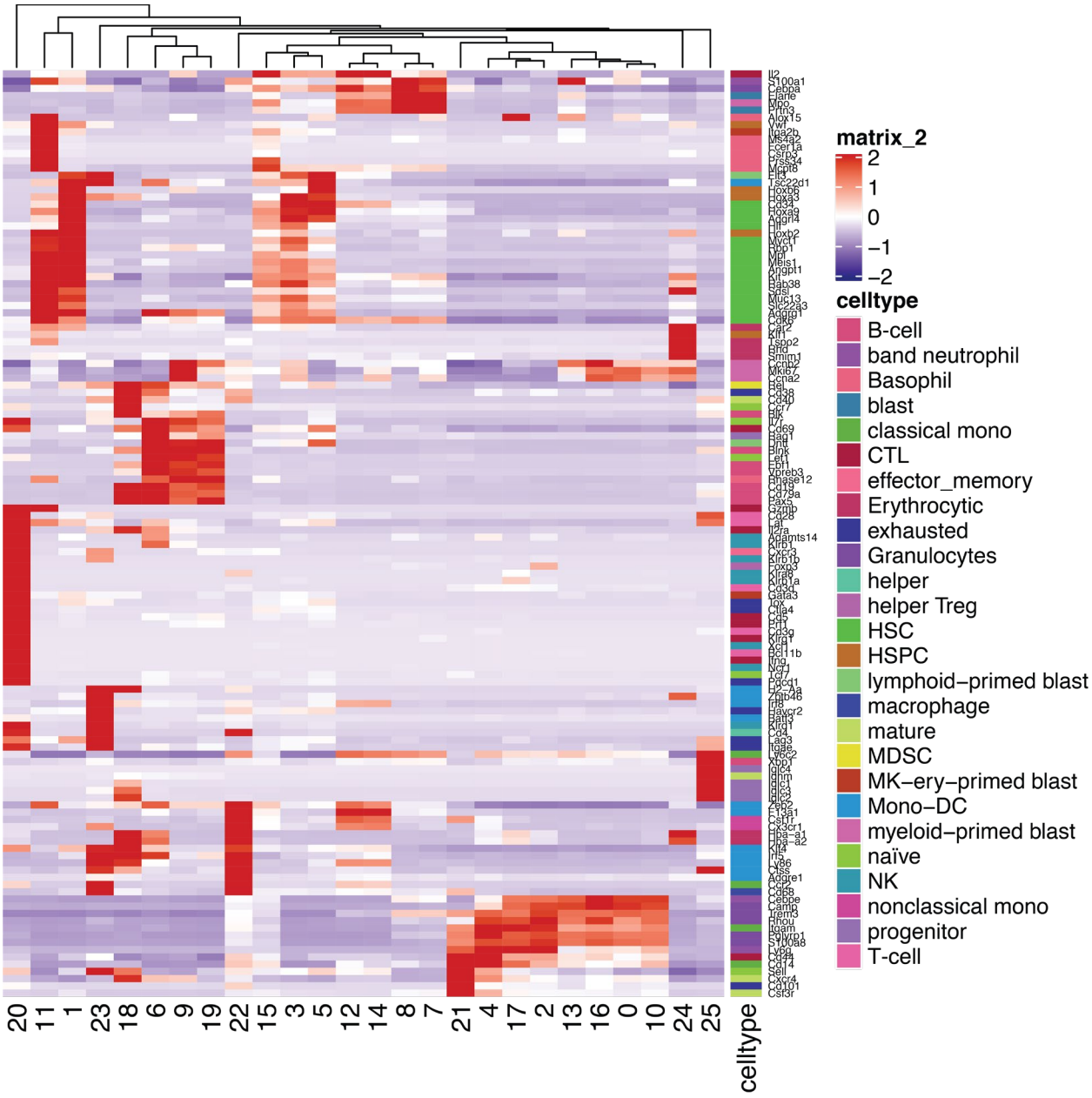

Supplemental Figure 6. scRNA-seq analysis of mouse bone marrow upon ^{223}Ra treatment. Heatmap showing the expression of 86 selected genes associated to distinct cell clusters based on literature findings. Based on common branching, the clusters were collapsed to 16 individual populations (Fig 4B).

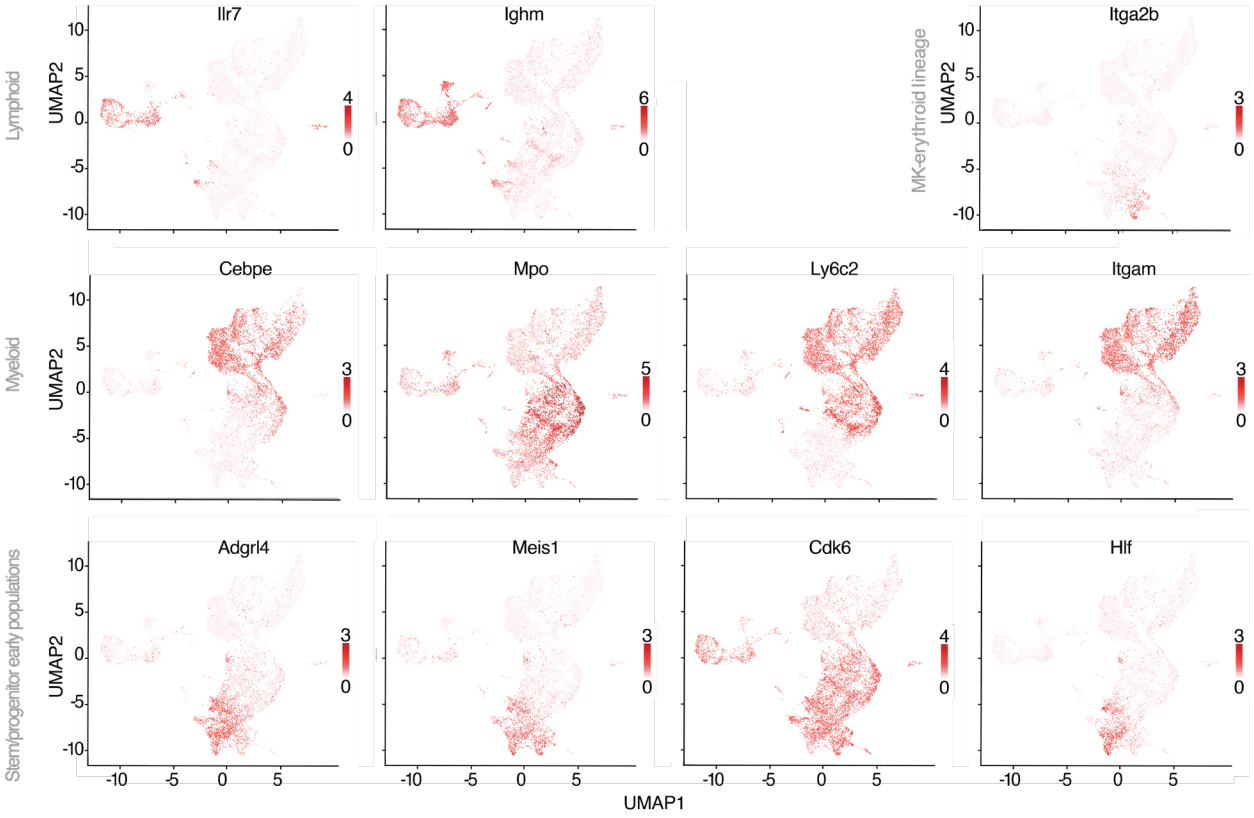

Supplemental Figure 7. scRNA-seq analysis of mouse bone marrow upon ^{223}Ra treatment. Feature plots for marker genes of stem/progenitor early populations or populations primed towards the myeloid, lymphoid and MK-erythroid lineage.

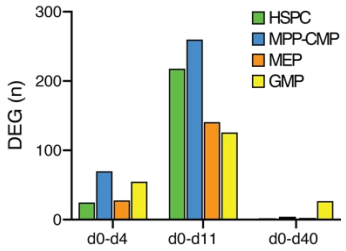

Supplemental Figure 8. Differentially expressed genes in stem cells and early progenitors. The total number of differentially expressed genes in mice treated with ^{223}Ra at day 4, 11 and 40 post-treatment versus untreated (d0) is shown.